



HAL
open science

Kinetics of hydrogen desorption from Zircaloy-4: Experimental and Modelling

Clara Juillet, Marc Tupin, Frantz Martin, Quentin Auzoux, Clément Berthinier, Frédéric Miserque, Fabrice Gaudier

► **To cite this version:**

Clara Juillet, Marc Tupin, Frantz Martin, Quentin Auzoux, Clément Berthinier, et al.. Kinetics of hydrogen desorption from Zircaloy-4: Experimental and Modelling. *International Journal of Hydrogen Energy*, 2019, 44 (39), pp.21264-21278. 10.1016/j.ijhydene.2019.06.034 . cea-02465182

HAL Id: cea-02465182

<https://cea.hal.science/cea-02465182>

Submitted on 20 Jul 2022

HAL is a multi-disciplinary open access archive for the deposit and dissemination of scientific research documents, whether they are published or not. The documents may come from teaching and research institutions in France or abroad, or from public or private research centers.

L'archive ouverte pluridisciplinaire **HAL**, est destinée au dépôt et à la diffusion de documents scientifiques de niveau recherche, publiés ou non, émanant des établissements d'enseignement et de recherche français ou étrangers, des laboratoires publics ou privés.



Distributed under a Creative Commons Attribution - NonCommercial 4.0 International License

Kinetics of hydrogen desorption from Zircaloy-4: Experimental and Modelling

C. Juillet⁽¹⁾, M. Tupin⁽²⁾, F. Martin⁽¹⁾, Q. Auzoux⁽¹⁾, C. Berthinier⁽³⁾, F. Miserque⁽¹⁾, F. Gaudier⁽⁴⁾

(1) Den-Service de la Corrosion et du Comportement des Matériaux dans leur Environnement (SCCME), CEA, Université Paris-Saclay, F-91191, Gif-sur-Yvette, FRANCE

(2) Den-Service d'Etude des Matériaux Irradiés (SEMI), CEA, Université Paris-Saclay, F-91191, Gif-sur-Yvette, France

(3) Den-Service d'Etude Mécaniques et Thermiques (SEMT), CEA, Université Paris-Saclay, F-91191, Gif-sur-Yvette, FRANCE

(4) Den-Service de Thermohydraulique et de Mécanique des Fluides (STMF), CEA, Université Paris-Saclay, F-91191, Gif-sur-Yvette, France

Keywords: Hydrogen; Desorption kinetics; Zirconium alloys; Thermal desorption mass spectrometry; Numerical modelling

1 Abstract

Under Pressurized Water Reactor normal operating conditions, the external surface of zirconium alloys cladding absorbs a fraction of the hydrogen produced by water reduction. During spent fuel transport, hydrogen may desorb from the cladding. The study aims to identify and quantify the rate-limiting step in the hydrogen desorption process initially present in the alloy. To better understand this process, the Thermal Desorption Spectrometry (TDS) was used in association with X-ray Photoelectron Spectroscopy analysis. TDS results were analyzed with finite elements simulations using the Cast3M code. The optimization of the kinetic constants of hydrogen desorption was performed with CEA (Alternative Energies and Atomic Energy Commission)-tool URANIE. Results showed that hydrogen desorption kinetics from the metal is limited by the surface molecular recombination. Arrhenius-type temperature dependence of kinetic constants allowed to simulate experimental data with a good agreement. The optimized activation energy and the pre-exponential factor for desorption processes were in the range of $290 \pm 10 \text{ kJ mol}^{-1}$ and $3 \times 10^7 \text{ m}^4 \text{ mol}^{-1} \text{ s}^{-1}$ respectively.

2 Introduction

In nuclear pressurized water reactors, ternary fission occurring within the uranium oxide fuel leads to the formation of tritium. Part of this tritium can then potentially diffuse from the fuel rod through the cladding and be released in the primary water, contributing to its radioactive contamination. During drying, transport, reprocessing or storage of used nuclear fuels, part of this tritium may also be released. A closer understanding of tritium transport phenomena, the quantification of their kinetics and a robust modelling of it are key parameters for a better estimation of potential tritium release. Tritium transport through the cladding includes tritium molecular adsorption and dissociation at the inner surface of the cladding, made of zirconium alloys, diffusion through the cladding and desorption or dissolution at the outer side of the cladding. As tritium transport involves many elementary steps, the global kinetics of tritium release in primary water will be controlled by the rate-limiting step. The aim of the present study, in the long term, is to identify and quantify the rate-limiting step in the permeation process of tritium (or hydrogenated species) through usual cladding materials such as Zircaloy-4 (referred to as Zy4 thereafter). The complexity of the system relies on the fact that the cladding material exposed to primary water is continuously oxidized during its lifetime, promoting hydrogen entry in the zirconium alloy from the outer side, while it is also oxidized on its inner surface due to residual water interactions or uranium oxide/zirconium redox reactions, and exposed to the tritium source [1]. It was therefore decided to first simplify the problem by studying a less complex system: the present work focuses on the transport and desorption processes of hydrogen in and from a Zy4 sheet unexposed to primary water. Therefore, the only source of hydrogen considered here is internal hydrogen, coming from the elaboration process. However, this simple system is more complex than it seems. Even at room temperature, a native oxide layer (a few nanometers thick) forms instantaneously on the surface of zirconium alloys, due to the high affinity of zirconium for oxygen and its low redox potential [1–3]. This thin oxide layer may reduce hydrogen release from the alloy, due to different diffusion kinetics in the oxide [4] and to different surface features as compared to the alloy, impacting adsorption states of hydrogen [5,6]. The hydrogen release from the bulk alloy can be decomposed into five elementary steps:

1. Diffusion of hydrogen atoms through the metallic part towards the metal/oxide interface, generally via interstitial sites [7];
2. Integration within the oxide lattice by crossing the metal/oxide interface;
3. Diffusion through the oxide towards the subsurface;

4. Passing from subsurface sites to surface sites as adsorbed species;
5. Final recombination into dihydrogen molecules and desorption in gas form from the oxide surface.

The hydrogen diffusion process through the α -Zr matrix has been widely investigated in the past [8–15] leading to a thorough estimation of the hydrogen diffusion coefficient in the zirconium alloys. The alloying elements do not seem to impact the diffusion coefficient of hydrogen. The diffusion coefficient is a function of temperature and follows an Arrhenius law. The average diffusion coefficient of hydrogen through the α -Zr matrix, deduced from the references [8–15], is expressed as follows :

$$D_{H_Zr} = D_{H_Zr}^0 \cdot \exp\left(-\frac{E_a}{RT}\right) = 10^{-7} \cdot \exp\left(-\frac{35000}{RT}\right) \quad (\text{m}^2 \text{ s}^{-1}) \quad (\text{Eq. 1})$$

Where $D_{H,Zr}^0$ englobes diffusion entropy change and jump probability, E_a corresponds to the migration enthalpy (in J), T is the temperature (in K) and R the ideal gaz constant ($8.314 \text{ J K}^{-1} \text{ mol}^{-1}$). The hydrogen diffusion coefficient in the zirconium alloys is equal to $10^{-7} \text{ cm}^2 \text{ s}^{-1}$ at 573 K. The values of $D_{H,Zr}$ given in the literature [8–15] in the 400 – 900 K temperature range are rather well gathered, unlike the diffusion coefficient determined in the oxide layer grown on zirconium alloys for hydrogen species. Indeed, the latter is susceptible, for a given temperature, to vary of many orders of magnitude, for instance between 10^{-17} and $10^{-14} \text{ cm}^2 \text{ s}^{-1}$ at about 573 K [4,16]. Such variability is due to many factors. The measurement of the diffusion coefficient depends indeed on the experimental procedure (isotopic exposure followed by SIMS or NRA analyses, hydrogen implantation followed by NRA analyses...), the environment (H_2O liquid or vapour, D_2O , H_2 , D_2) and the material (Zr, Zr₄ and Zr-2.5Nb...).

Furthermore the apparent hydrogen diffusion coefficient through the oxide layer deduced from permeation or release experiment [15,17] is also 1 or 2 orders lower than the ones measured by absorption during the corrosion process or diffusion after hydrogen implantation. The hydrogen diffusion in the oxide is lower compared to the hydrogen diffusion in the alloy.

Concerning the recombination step of hydrogen at the surface, the theoretical model proposed by Baskes [18] calculates the kinetics constants of this step from different metallic substrates. The value obtained from this model is basically equal to $+10^{-24} \text{ at}^{1/2} \text{ cm}^2 \text{ s}^{-1}$ at 773 K for zirconium. This value of the kinetic constant found in reference [18] will afterwards be compared with that measured during this study. This low value of kinetics constants suggest that surface recombination on zirconium could be slow enough not to be neglected in the global hydrogen release kinetics.

Based on thermal desorption spectrometry and nuclear reaction analysis on titanium, Wilde [19] proposes a schematic one-dimensional energy diagram visualizing the kinetic barriers encountered by H atoms chemisorbed on a metal surface for the competing reactions of recombinative desorption and bulk absorption. It assumes that the hydrogen desorption is limited by the surface recombination step.

As the kinetic constants for each transport step of hydrogen from bulk alloy to dihydrogen surface recombination and desorption (enumerated above from 1 to 5) are not all reported in literature nor sufficiently documented, one identifies a need for assessment of the rate limiting step for the global reaction and its kinetics, starting from the simple case of an unoxidized specimen. The impact of the presence of significant oxide layer (pre-oxidized specimen) stands outside the limit of the present paper and will need further dedicated works.

To reach this goal, the Thermal Desorption Spectrometry (TDS) technique was extensively used to study hydrogen kinetics desorption [20,21] in association with X-ray Photoelectron Spectroscopy (XPS) analyses. XPS analyzes enable to follow the evolution of the oxide layer during the desorption experiment. The TDS results were analysed thanks to simulations by finite elements (FE) using the Cast3M code [22,23] and the optimization of the kinetic constants has been performed with URANIE tool developed at CEA. This tool is based on the “root” platform developed in the European Organization for Nuclear Research Center [24].

3 Experimental Procedure

3.1 Material and specimen preparation

0.45 mm sheets of recrystallized Zircaloy-4 (Zy4) supplied by FRAMATOME™ were used. The typical chemical composition of the alloy is given in Table 1. The specimens were cut from the sheet to 1 cm² specimens. For each specimen, both main sides were ground with SiC emery paper and submitted to a final polishing with ¼ µm diamond paste. The samples were then cleaned in acetone-ethanol solution and finally rinsed in deionized water and dried in air. The final thickness of the sample was around 350 µm.

Table 1. Typical chemical composition of the Zircaloy-4 alloy (wt.%).

Alloying elements	Fe	Cr	Sn	O	H wt. ppm	Zr
-------------------	----	----	----	---	-----------	----

Zircaloy-4	0.18 – 0.24	0.07 – 0.13	1.2 – 1.5	0.10 – 0.14	20 – 30	Bal.
-------------------	-------------	-------------	-----------	-------------	---------	------

3.2 Thermal Desorption Spectrometry

The desorption kinetics of hydrogen are determined by thermodesorption. The Thermal Desorption Spectrometry (TDS) set-up used in this study, developed at CEA, is made of a quartz tube under vacuum (10^{-6} – 10^{-7} mbar) wherein the specimen is inserted, surrounded by a cylindrical furnace coupled to a quadrupole mass spectrometer (Transpector 100-M INFICON™). By imposing an external temperature ramp (by means of the tubular furnace), the specimen is heated up and volatile solutes or adsorbates tend to desorb during heating. Desorbed species are then ionized, separated, detected and counted (ion current) by the mass spectrometer. Hydrogen for instance can therefore be detected and eventually quantified. The investigated temperature range is between 298 K to 1273 K. Calibrated $^2\text{H}_2$ leaks were used to calibrate the ion current corresponding to hydrogen species and convert it into molar flux. TDS results regarding other desorbing species were not quantified. The amount of hydrogen desorbed from the specimen in the course of the TDS experiment was estimated by integration of this calibrated signal as function of the time during the experiment.

3.3 X-Ray Photoelectron Spectroscopy

X-ray photoelectron spectroscopy (XPS) analyses were carried out with a Thermofisher Scientific ESCALAB 250xi using a monochromatic X-ray Al-K α source ($h\nu = 1486.6$ eV). The XPS analyzes make it possible to follow the evolution of the oxide layer during the TDS temperature ramp. The analysis zone consisted in a 900 μm diameter spot. The data processing was performed using the commercially available Avantage™ software, which permitted to estimate the oxide layer thickness.

4 Results and discussion

4.1 Thermal desorption spectrometry experiments

Figure 1 shows the hydrogen desorption thermogram (red circles) obtained on an as-prepared Zircaloy-4 specimen. This TDS experiment was carried out with a 10 K min^{-1} temperature ramp from 293 K up to 1273 K. Focus was made on two m/z ratio, 2 and 18 corresponding to dihydrogen and water molecules respectively.

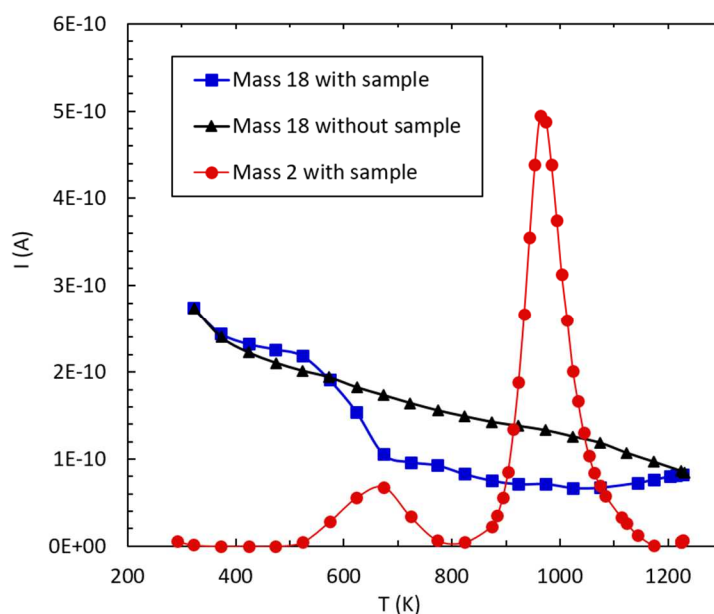


Figure 1. TDS spectra obtained for a temperature ramp of 10 K min^{-1} : the signals corresponding to $m/z = 2$ (H_2) and $m/z = 18$ (H_2O) with the specimen in the analysis chamber appear in blue and red, the signal of $m/z = 18$ without any sample appears in black.

For hydrogen, two desorption peaks were observed: one centered around 673 K and the second one at higher temperature, located around 973 K. According to literature dealing with TDS thermograms analysis, each peak should theoretically be assigned to a type of interaction of hydrogen with the material (interstitial site, trapping at defects etc.) [25–28]. The aim of the following sections is to determine to which kind of interaction the two peaks shown in Figure 1 do correspond.

Figure 1 also describe the evolution of the water molecule desorption flux for an experiment with a sample in the furnace and another one without any specimen, respectively. Both flux decrease during heating, showing the effect of continuous pumping of water desorbing from the set-up and vacuum quality improvement. The sharper decrease in the water molecules flux observed in the 573-673 K range in presence of the specimen, as compared to the blank (without specimen) suggests a consumption of water molecules during the course of temperature ramping. Knowing the high reactivity of zirconium and its alloys regarding water or oxygen, even at very low partial pressures [29,30], we suggest that this water consumption may result from zirconium oxidation by residual water within the set-up, thus forming an oxide layer on the specimen surface. Meanwhile, water reduction leads to the formation of dihydrogen molecules. The first peak observed on the H_2 ($m/z = 2$, red circles) signal in the thermogram shown in Figure 1, occurring in the same range of temperatures could therefore result from this reduction.

This interpretation was challenged thanks to the following TDS experiment: a Zy4 specimen was introduced in the set-up and first heated at 10 K min^{-1} up to 773 K (below the temperature at which the second desorption peak occurs), cooled down to room temperature and then heated again at 10 K min^{-1} up to 1273 K with continuous pumping during the whole experiment duration. Figure 2a and Figure 2b present, respectively, the evolutions of the hydrogen signal and of the H_2O signal detected by the mass spectrometer during the first (black dots) and second (red squares) temperature ramps. Black curves (first temperature ramp) present similar features than in Figure 1, showing a good reproducibility of the results. Red curves (second temperature ramp) do not show any sharp decrease of the H_2O signal, nor concomitant H_2 peak, in the 573-673 K range. These observations agree with the hypothesis of dihydrogen production resulting from Zy4 oxidation by residual water molecules present in the set-up (vacuum and/or adsorbed on the quartz tube walls) prior to temperature ramping: after the first ramp, most of the water molecules have desorbed and reacted; no oxidizing species are available any more during the second ramp. As a consequence, the first hydrogen desorption peak was assigned to the reaction of reduction of water associated with Zy4 oxidation, following global reaction (Eq. 2) [31].

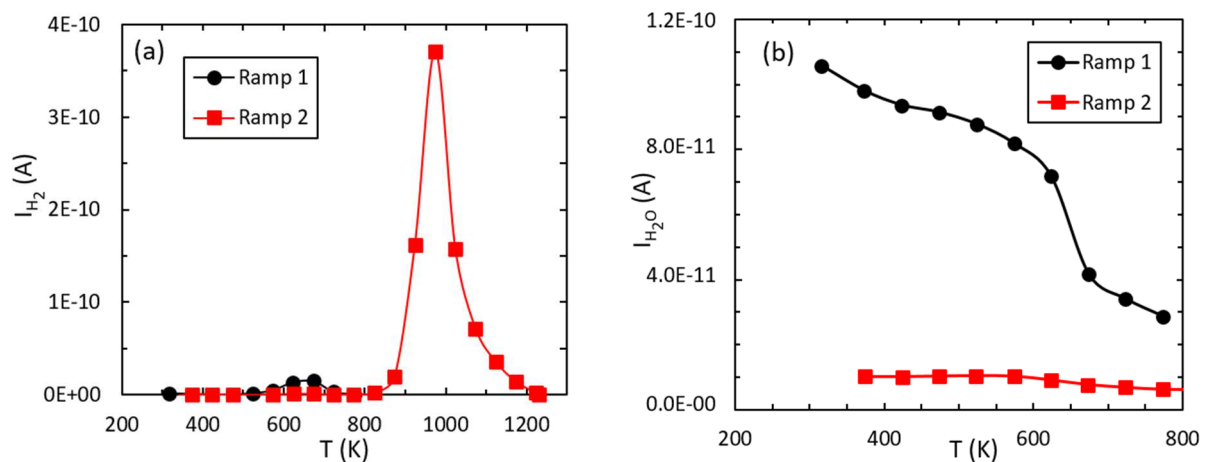
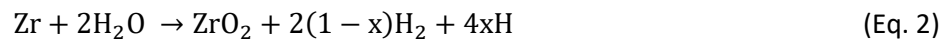


Figure 2. TDS spectra detected during the first (black) and the second (red) temperature ramps at 10 K min^{-1} : (a) H_2 signal; (b) H_2O signal.

Note that in (Eq.2), a part of the hydrogen produced by water reduction is absorbed by the alloy (“ $4x\text{H}$ ”).

The second hydrogen desorption peak was assigned to hydrogen desorption from the alloy itself. Discussions on this high temperature peak and more TDS results will be provided further away in the paper.

Besides, a rough estimation of the oxide layer thickness (δ) formed during the temperature ramp up to 773 K can be obtained by integrating the first peak of the spectrum and assuming x is equal to zero in (Eq.2). One obtains an oxide thickness estimate around 40 nanometers due to the oxidation process. The native oxide layer, initially present on the as-prepared specimens, is also to be taken into account. Investigation conducted into this surface oxide layer and its evolution in the course of the TDS experiment are described in the next section.

4.2 X-Ray Photoelectron Spectroscopy study of the surface oxide

The surface oxide thickness (δ) was estimated by XPS, thanks to a method detailed elsewhere [32]. The Zr-3d oxide-to-metal peak ratio (I_{ox}/I_{met} where I stands for the peak intensity) of the XPS spectrum was used to determine δ according to the relationship described in Eq.3.

$$\delta = \lambda_{ox} \cos(\theta) \ln \left(\frac{N_{met} \lambda_{met} I_{ox}}{N_{ox} \lambda_{ox} I_{met}} + 1 \right) \quad (\text{Eq. 3})$$

Where $\frac{N_{met}}{N_{ox}}$ is the ratio of the volume densities of Zr atoms in metal to oxide, θ is the angle between the normal of the sample surface and the analyzer (set at 0 K in this work), λ_{met} and λ_{ox} are the inelastic mean free paths (corresponding to the average distance of an electron between two inelastic collisions) in the metal and in the oxide, respectively. The mean free path values in metallic Zr and ZrO_2 were evaluated according to the TPP-model [33] : $\lambda_{met} = 2.6$ nm and $\lambda_{ox} = 2.3$ nm.

Figure 3 shows the XPS Zr-3d core levels spectrum obtained on a Zy4 sample after the final polishing. The Zr-3d oxide-to-metal peak ratio was approximately 7, leading to a calculated native oxide film thickness of 6.0 ± 0.5 nm.

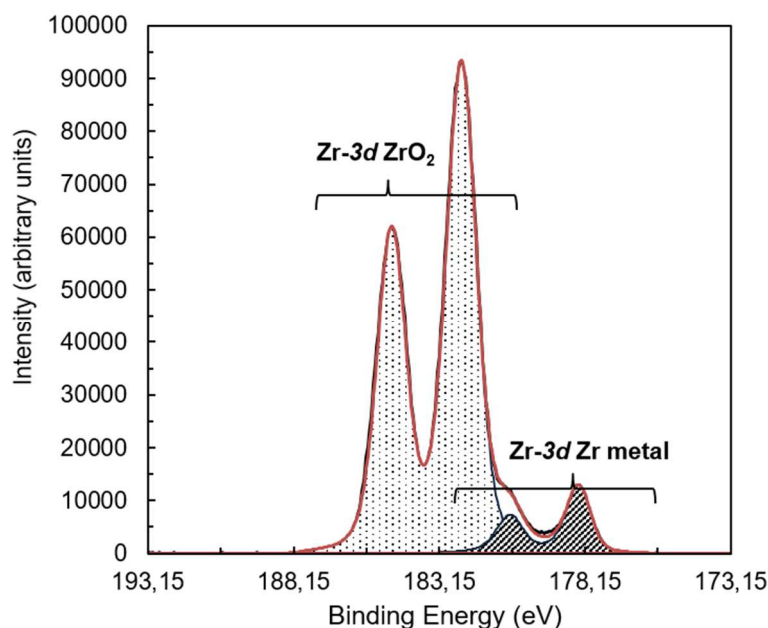


Figure 3. Zr-3d core levels spectrum obtained on a Zy4 sample with its native oxide layer. Zr-3d contributions assigned to ZrO_2 (dotted area) and metallic Zr (hatched area) were obtained by the fitting procedure.

Attempts to quantify by XPS the oxide thickness that was formed during the TDS temperature ramp were also made. A first TDS experiment was carried out with a 10 K min^{-1} temperature ramp from 293 K up to 673 K, at the maximum of the first peak of hydrogen desorption. A second TDS experiment, with an identical heating rate, terminated at 773 K, after the first peak, was conducted to reveal a hypothetical evolution of the oxide thickness with temperature increase in the TDS set-up.

Figure 4a and Figure 4b present the XPS Zr-3d core levels spectra after TDS experiments terminated at 673 K and 773 K, respectively. In Figure 4a, only the Zr-3d peak relative to oxidized zirconium is observed (mostly in ZrO_2): no metallic state (0 oxidation state) contribution was detected for the TDS terminated at 673 K. It means the oxide thickness is greater than the XPS analysis depth ($\sim 10 \text{ nm}$). After the interrupted TDS at 773 K, the Zr-3d peak relative to the metallic state contribution is detected (Figure 4b). The Zr-3d oxide-to-metal peak ratio (I_{ox}/I_{met}) is much smaller (approximately 0.5) than the one found for the native oxide (approximately $6.0 \pm 0.5 \text{ nm}$), revealing a very thin remaining oxide layer and a significant dissolution of the oxide layer. In Figure 4b the low binding energy contribution was assigned to both Zr and ZrC. The binding energy chemical shift between these two compounds is relatively small ($\sim 0.4 \text{ eV}$) [34] making their separation difficult. The presence of ZrC is suggested by the C-1s core level spectrum (not shown): a contribution at $281.9 \pm 0.3 \text{ eV}$ is noticed, which is characteristic of zirconium carbide compound [35].

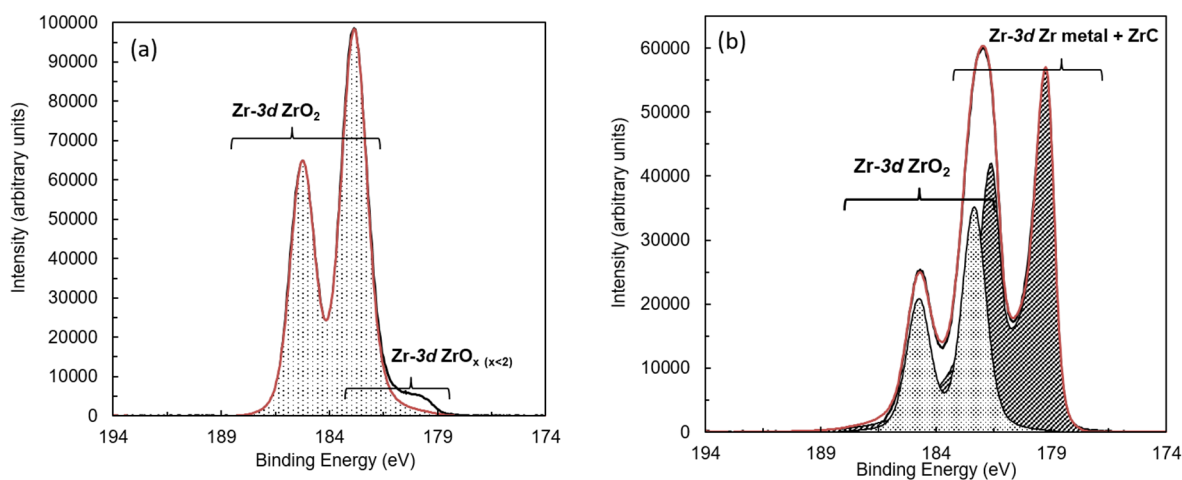


Figure 4. Zr-3d core levels spectra obtained on Zy4 samples after TDS experiments terminated at (a) 673 K and (b) 773 K. Zr-3d contributions assigned to ZrO_2 (dotted area) and metallic Zr or Zr carbide (hatched area) are used for fitting procedure.

These XPS results show that: (i) during the heating ramp up to 673 K, the oxide thickness on the Zy4 specimen in the TDS chamber increased, which is consistent with surface oxidation by residual water, and (ii) between 673 K and 773 K the oxide thickness decreased. The only possible explanation for the second point is ZrO_2 dissolution in the alloy [36]. Since some re-oxidation of the specimen surface by “in air” transition between TDS and XPS set-ups could have occurred, the following conclusion can be drawn regarding the effective presence of an oxide layer during the TDS experiment when temperature reached 773 K: either the oxide is absent or it is very thin.

A complementary XPS experiment was carried out on a Zy4 sample just after the final polishing. This sample was heated directly under vacuum ($\sim 10^{-9}$ mbar) in the XPS chamber at 3 K min^{-1} from 293 K up to 973 K. A lower heating rate than in the previous experiments is chosen in order to enhance the oxide scale dissolution and ensure acquisition time and good integration of the XPS signals (the lower the heating rate, the greater oxide dissolution). Figure 5 presents the atomic relative concentration of Zr, C (only the carbide contribution is considered in the quantification) and O obtained during this experiment and suggests a dissolution of the native oxide from 400 K.

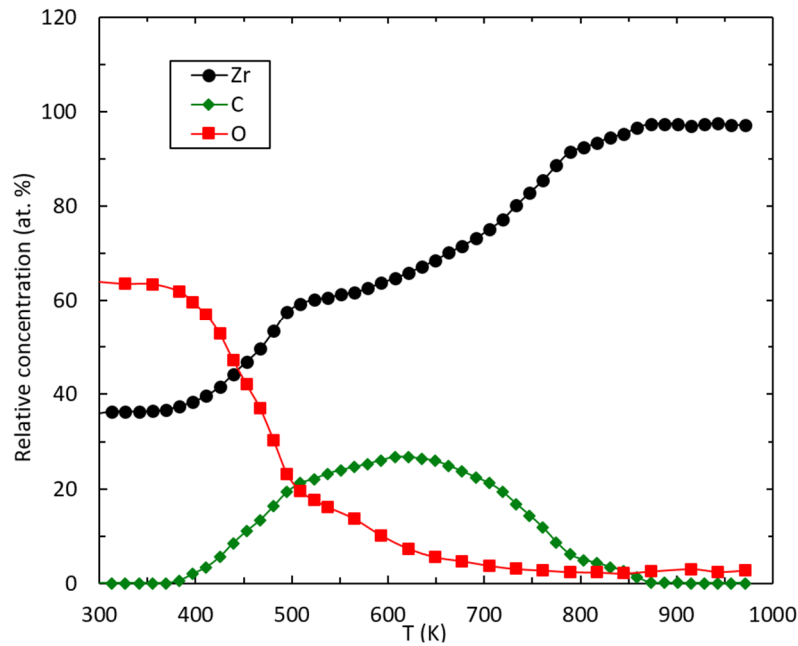


Figure 5. Relative concentration profiles of Zr (black circles), C (red diamonds) and O (red squares) in at.% during a temperature ramp at 3 K min⁻¹.

Beyond 673 K, the concentration is very low meaning that there is no more oxide at the surface. From 850 K the relative concentrations of Zr and O are constant; the native oxide is completely dissolved. During the temperature ramp, a high carbon concentration (approximately 25 at.%) appears at the extreme surface. These zirconium carbides are probably due to the reaction between the carbon of contamination present on the surface and in contact with the atmosphere and the various manipulations in air. It is noted that in quantification, the aliphatic carbon (C-C, C-H) present at the sample surface was not taken into account.

It is therefore not possible to conclude definitely about the total or partial dissolution of the oxide layer before the emergence of the second hydrogen desorption peak during the TDS experiment. For this reason, some calculations based on literature data were made to evaluate the oxygen dissolution in the Zy4 and to determine the surface state of the specimen just before the second TDS desorption peak observed for hydrogen. This represents a key point for the rest of the study, since it defines the boundary conditions of the system considered for hydrogen desorption process from Zy4 bulk: with or without an oxide layer.

4.3 Simulation of the oxygen dissolution and comparison with XPS and TDS experimental results

Oxygen dissolution in the α -Zr matrix has been extensively studied during the last decades [37–39], but mainly at high temperatures. During the dissolution of the oxide layer, the authors consider oxygen solubilization very easy. No barrier effect to the oxygen diffusion at the oxide/metal interface was noticed.

The dissolution of the oxide layer was modelled considering the oxide as an unlimited source of oxygen and that the oxygen concentration in the subsurface of the alloy was constant and equal to 30 at.%, which corresponds to the saturation concentration of oxygen in the α -Zr matrix. Based on these boundary conditions, Fick's second law was used to solve the oxygen transport in the alloy from its surface (subsurface). Due to the non-isothermal conditions of the TDS experiments, the analytical solution of Fick's second law could not be used. The dissolution process was solved numerically by finite elements (FE) using the Cast3M code [22,23]. The diffusion equation used in the Cast3M code is Fick's second law (Eq. 5):

$$\frac{\partial C_{O_Zr}}{\partial t} = \vec{\nabla} \cdot \left(D_{O_Zr} \vec{\nabla} (C_{O_Zr}) \right) \quad (\text{Eq. 5})$$

According to literature data [40], the oxygen diffusion coefficient is quite well known and is expressed as follows (Eq. 4):

$$D_{O_Zr} \cong 6 \times 10^{-5} \cdot \exp\left(-\frac{197237}{RT}\right) \quad (\text{m}^2 \text{s}^{-1}) \quad (\text{Eq. 4})$$

The actual temperature ramp obtained for a TDS experiment terminated at 773 K (corresponding to a theoretical ramp of 10 K min⁻¹) and two others TDS experiments terminated respectively at 813 K and 853 K (based on the TDS experiment terminated at 773 K) were injected in the FE code and the Fick's second law was solved for each case. The corresponding calculated oxygen concentration profiles after the three above-mentioned ramps including the cooling down to room temperature (we considered the same cooling down for the three TDS experiments) are presented in Figure 6.

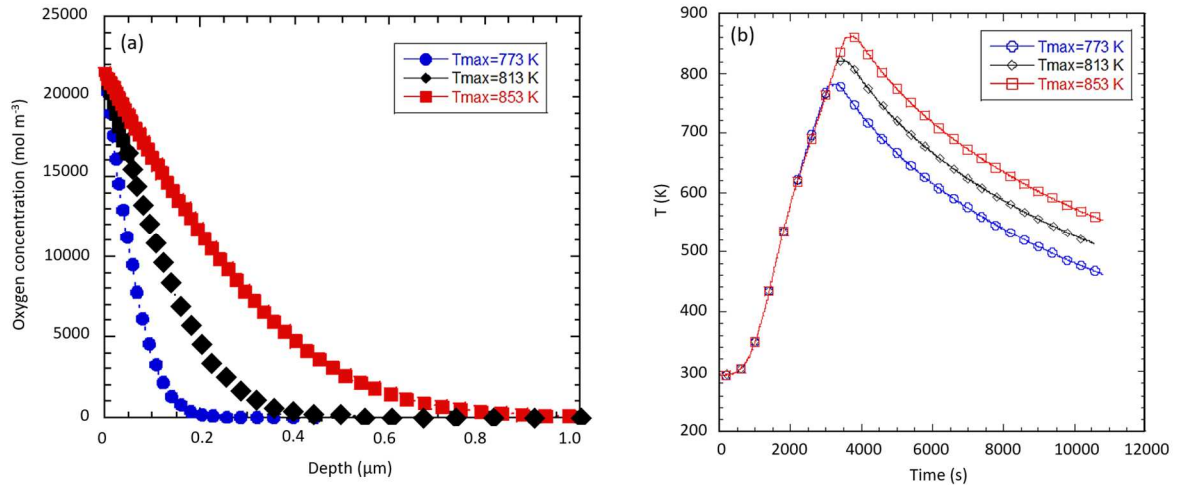


Figure 6. (a) Calculated oxygen concentration profiles (dots) in the alloy after a 10 K min⁻¹ temperature ramp up to 773 K (blue circles), 813 K (black diamonds) and 853 K (red squares), respectively; (b) corresponding temperature ramp.

Calculated oxygen penetration depth increases strongly with the maximum temperature. The amount of oxygen dissolved into the alloy during these thermal annealings, $n_{O,total}$, was evaluated by integrating the simulated oxygen profiles. Results for 3 K min⁻¹ and 10 K min⁻¹ ramp rates are gathered in Table 2.

Table 2. Oxygen amount per unit area (mol m⁻²) dissolved in the alloy during various temperature ramps up to 773, 813 and 853 K, respectively.

Ramp test	T _{max} = 773 K	T _{max} = 813 K	T _{max} = 853 K
$n_{O,total}$ (mol m ⁻²) (10 K min ⁻¹)	1.28x10⁻⁷	2.76x10⁻⁷	5.59x10⁻⁷
$n_{O,total}$ (mol m ⁻²) (3 K min ⁻¹)	1.13x10⁻⁷	2.50x10⁻⁷	5.15x10⁻⁷

The dissolved oxygen amounts are relatively close whatever the ramp rate. The difference is due to the higher temperature overshoot for the highest ramp: the effective temperature maximum was around 10 K higher than that obtained for the lowest ramp.

The objective here is to estimate, with a 10 K min⁻¹ heating rate, whether at the temperature at which the second hydrogen desorption peak occurs the surface is still covered by an oxide layer, and estimate its thickness. In previous calculations, the source of oxygen supplied by the oxide layer was supposed infinite. As was estimated in previous section, the oxide layer thickness is finite and

reaches 40 nm. This corresponds to an amount of available oxygen that can be calculated from following formula (Eq. 6):

$$n_{O_ZrO_2} = 2 \times 40 \times 10^{-9} \times \frac{\rho_{ZrO_2}}{M_{ZrO_2}} \quad (\text{Eq. 6})$$

with ρ_{ZrO_2} the density of the monoclinic zirconia (5.6 g cm⁻³), M_{ZrO_2} the molar mass of zirconia (123 g mol⁻¹) and $n_{O_ZrO_2}$ the amount of oxygen in the zirconia layer per unit area, expressed in mol m⁻². The corresponding oxygen amount is basically 3.64 x 10⁻⁷ mol m⁻² for a 40 nm thick oxide layer. Comparing this value with those in Table 2, one sees that at 853 K, the oxide layer has fully been dissolved but may remain at 773 K and 813 K.

In addition, one also has to take into account that part of the oxygen that was in the oxide layer that has dissolved remains in the newly formed “oxygen –saturated alloy” in place of the former oxide layer, representing 30 at.% of oxygen in this “new” matrix. Assuming a Pilling-Bedworth ratio (PBR) of 1.56 between ZrO₂ and Zr alloy, one can assume that 40 nm oxide corresponds to 26 nm alloy saturated with O. The oxygen amount in this part, which has not contributed to diffusion in the matrix towards the bulk, can be estimated by the following formula (Eq.7):

$$n_{O_Zr} = 26 \times 10^{-9} \times 0.3 \times \frac{\rho_{Zr}}{M_{Zr}} \quad (\text{Eq. 7})$$

with ρ_{Zr} the density of α -Zr (6.5 g cm⁻³) and M_{Zr} the atomic mass of zirconium. The oxygen quantity remaining in the metal in place of the formerly present oxide layer is 0.56 x 10⁻⁷ mol m⁻². The corrected amount of oxygen inserted in the alloy during the dissolution of a 40 nm thick zirconia layer is thus 0.56 x 10⁻⁷ mol m⁻².

By comparing the values given in Table 2 with the difference between the amounts given by the equations (Eq. 6) and (Eq. 7) equal to 3.08 x 10⁻⁷ mol m⁻², we found that the oxide layer is almost completely dissolved with a 10 K min⁻¹ or 3 K min⁻¹ heating rate after the ramp stopped at 813 K and definitely dissolved for the ramp up to 853 K. However, at 773 K this calculation shows that the third of the oxide layer has approximately disappeared.

These first order calculations tend to show that at 853 K with a 10 K min⁻¹ heating rate, *i.e.* at the very beginning of the second hydrogen desorption peak in the TDS experiments, the oxide layer formed during the first part of the experiment has completely disappeared by dissolution in the alloy matrix. Good agreement with XPS analysis on TDS is obtained. Beyond 853 K, the studied system becomes finally very simple as it can be considered as purely metallic and only hydrogen bulk diffusion in the

alloy, hydrogen transition from subsurface to surface as adsorbate and surface adsorption/desorption reaction have to be taken into account, as illustrated by the sketch in Figure 7.

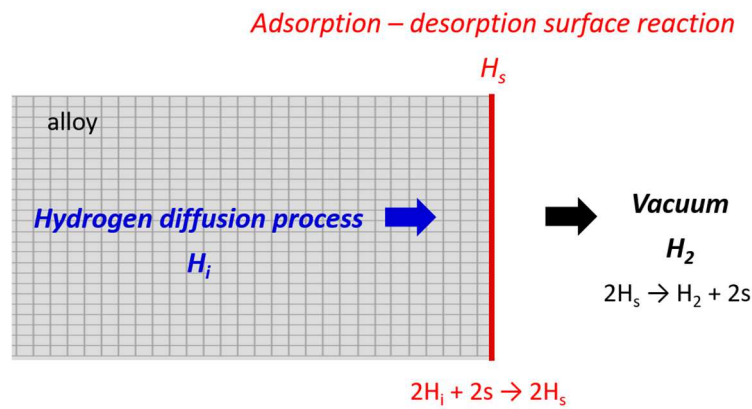


Figure 7. Sketch of the system considered for hydrogen release from the alloy at temperatures above 853 K.

4.4 Modeling of the hydrogen desorption kinetics and identification of the desorption rate-limiting step

4.4.1 Preface

As previously mentioned, in the experimental conditions of the present study, the hydrogen desorption mechanism can be reduced to three steps:

1. The hydrogen diffusion inside the Zy4 specimen;
2. Hydrogen transition from subsurface to surface as adsorbate;
3. The adsorption-desorption reaction occurring on the surface.

The objective here is to identify the rate-limiting step for global desorption from the alloy and to determine the associated rate constant and its dependence with temperature. The second step (subsurface to surface transport) was assumed to be rapid compared with the third one. In other words, it is considered to be in equilibrium. In this case, the hydrogen surface covering rate is assumed proportional to the interstitial hydrogen concentration near the surface. The system is hereby reduced to two possible rate-limiting steps, *i.e.* (1) or (3).

As recalled in the introduction, the hydrogen diffusion coefficient D_{Hi} in the α -Zr matrix is well documented and relevantly described by equation (Eq. 1). This expression of D_{Hi} was used as input

data in the FE code (Cast3M) for all simulations. The diffusion equation used in the Cast3M code is Fick's second law:

$$\frac{\partial C_{H_i}}{\partial t} = \vec{\nabla} \cdot \left(D_{H_i} \overrightarrow{\nabla}(C_{H_i}) \right) \quad (\text{Eq. 8})$$

where C_{H_i} represents the concentration of hydrogen atom in interstitial positions inside the α -Zr lattice and D_{H_i} , the hydrogen diffusion coefficient in the alloy (*i.e.* from an interstitial site to another).

The recombination process of hydrogen at the surface is described by the following elementary step (Eq. 9):



with H_i an interstitial hydrogen atom in subsurface, V_i a free interstitial site in the hcp lattice, and H_2 a dihydrogen molecule released in vacuum.

The hydrogen recombination rate at the surface is given by the following expression (Eq. 10):

$$r_{H_2} = k'_{des}(C_{H_i})^2 - k'_{ad} \left(\frac{P_{H_2}}{P^0} \right) (C_{f_i})^2 \quad (\text{mol m}^{-2} \text{ s}^{-1}) \quad (\text{Eq. 10})$$

where C_{f_i} and C_{H_i} are, respectively, the volume density of the free interstitial sites and the concentration of interstitial hydrogen at the surface (mol m^{-3}), k'_{ad} and k'_{des} are the adsorption/desorption rate constants for each process ($\text{m}^4 \text{ mol}^{-1} \text{ s}^{-1}$) and P_{H_2} the hydrogen pressure in contact with the metal (Pa), and P^0 a reference pressure (Pa).

In the framework of this work, P_{H_2} was assumed very small due to continuous pumping and secondary high vacuum in the TDS chamber (below 10^{-6} mbar) and taken as tending towards zero. In other words the second term is neglected during the desorption process.

However, the hydrogen desorption rate entered in Cast3M code is not exactly the same as (Eq.10). It is indeed expressed, for numerical commodity, as follows (Eq. 11):

$$\varphi_{H_2} = \frac{k_{des}}{2C_H^{init}} (C_{H_i})^2 \quad (\text{mol m}^{-2} \text{ s}^{-1}) \quad (\text{Eq. 11})$$

with C_H^{init} , the initial hydrogen concentration in the metal and k_{des} , a desorption rate constant expressed in m s^{-1} , and linked to the k'_{des} rate constant according to the following formula (Eq. 12):

$$k_{des} = 2C_H^{init}k'_{des} \quad (\text{Eq. 12})$$

Note that unlike k'_{des} , k_{des} is function of the initial hydrogen concentration.

Two options were considered in order to reach our objective, which are the subject of next sections: (i) the desorption rate is limited by diffusion in the bulk and (ii) the desorption rate is limited by surface recombination.

4.4.2 Hydrogen diffusion in the metal as desorption rate-limiting step

The present study was carried out without any hydrogen charging of the Zy4 samples, only the hydrogen resulting from the elaboration process, present as hydride in the as-received material was used (approximately 24 wt. ppm). Une and Ishimoto determined a terminal solid solubility during the dissolution of 20 wt.ppm at 473 K [41]. In the rest of the study, hydrogen will therefore be considered in solid solution.

In order to ensure a diffusion-limited desorption rate, one had to impose an infinitely high recombination kinetic constant whatever the temperature. A value for k_{des} was arbitrarily chosen as $k_{des} = 1.63 \times 10^5 \exp\left(-\frac{110000}{RT}\right) \text{ m s}^{-1}$ in this section. This constant is three orders of magnitude greater than the hydrogen desorption flux. All desorption flux calculations were made using an initial homogeneous and uniform distribution of hydrogen in the Zy4 with an average concentration of 24 wt. ppm (*i.e.* 156 mol m⁻³). Both experimental and simulated data of hydrogen desorption flux as function of temperature are shown in Figure 8. According to findings mentioned in section 3.1 to 3.3, the first experimental peak is not to be reproduced by the simulation since it was not assigned to desorption from the alloy. We always refer to the high temperature peak when comparing experimental data to simulation ones.

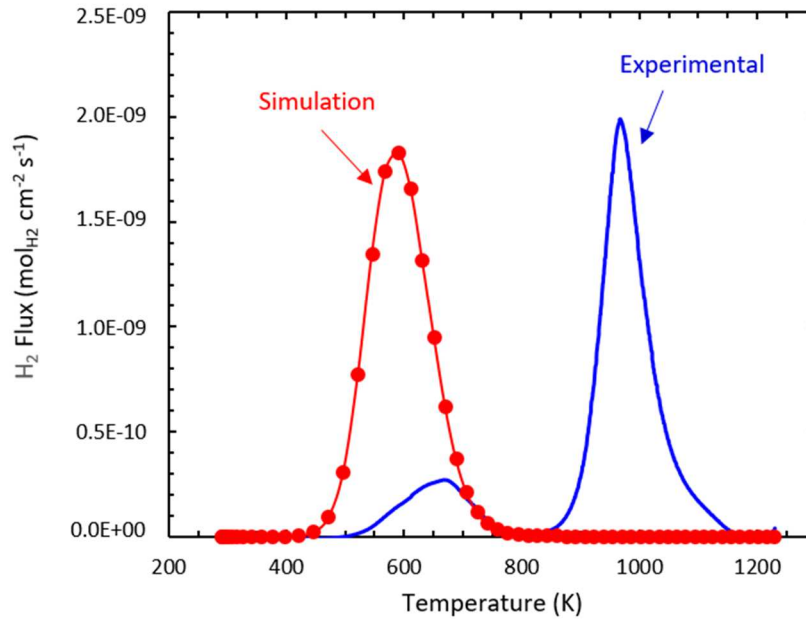


Figure 8. Comparison of the H₂ fluxes obtained experimentally by TDS (blue squares) and by FE simulation of a purely diffusion-controlled desorption rate (red circles).

The simulated hydrogen desorption flux (red circles in Figure 8) is undoubtedly far away from the experimental second peak of the TDS spectrum (blue dots in Figure 8). Clearly, the TDS thermogram cannot be correctly simulated by assuming only a diffusion-controlled desorption of hydrogen from the Zy4 specimens. It can be noted that the diffusion coefficient of hydrogen through the α -Zr matrix [8–15] is independent of the microstructure, the alloying elements (pure zirconium, Zircalloys, Zr-Nb) and the precipitates ($Zr(Fe,Cr)_2$, β -Nb). Therefore trapping phenomenon is assumed negligible. The option (ii), surface recombination, was therefore the only possibility to be a rate-controlling step.

4.4.3 Surface hydrogen recombination step as desorption rate-limiting step

The desorption peaks (TDS experiments) depend on the temperature ramp rate. TDS experiments at different heating rates were carried out. Some experiments were repeated twice. Figure 9 represents the influence of the ramp rate on the hydrogen desorption flux as function of temperature. These tests were used to determine the activation energy of hydrogen desorption using the Choo-Lee plots [25].

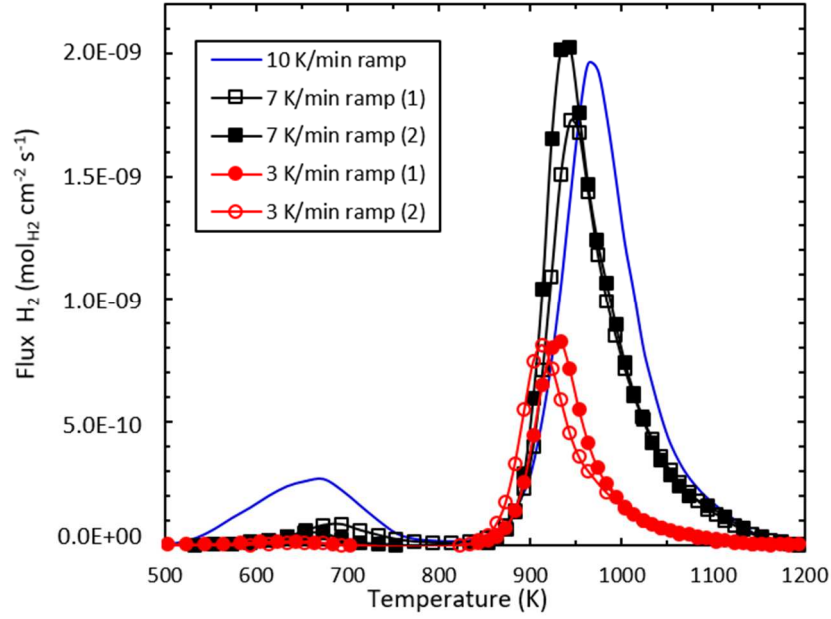


Figure 9. TDS spectra obtained for signals corresponding to mass 2 (H_2) for a temperature ramp of: 10 K min^{-1} (blue line), 7 K min^{-1} (black squares), 3 K min^{-1} (red circles).

By increasing the heating rate, the peaks are shifted towards high temperatures, as shown in Figure 9. Using the temperature T_m at which the maximum hydrogen release occurs, the Choo-Lee representation consists in plotting $\ln\left(\frac{\Phi}{T_m^2}\right)$ versus $1/T_m$ with Φ , the ramp rate. The activation energy is given by the following Kissinger's expression at the first order [42] (Eq. 13):

$$Ea_{des} = -R \frac{\partial \ln\left(\frac{\Phi}{T_m^2}\right)}{\partial \left(\frac{1}{T_m}\right)} \quad (\text{Eq. 13})$$

where R is the ideal gas constant ($8.314\text{ J K}^{-1}\text{ mol}^{-1}$) and ϕ the heating rate (K min^{-1}).

Figure 10 depicts the evolution of $\ln\left(\frac{\Phi}{T_m^2}\right)$ as a function of the inverse of T_m . The desorption activation energy is calculated from the slope of the linear curve.

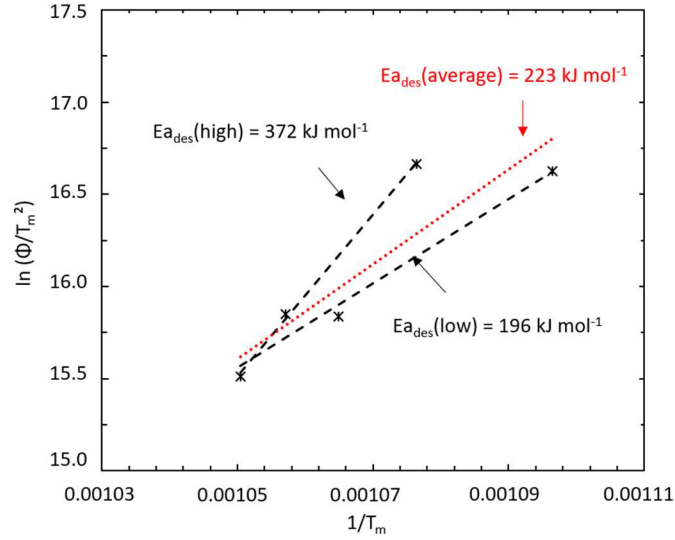


Figure 10. Choo-Lee representation: $\ln\left(\frac{\Phi}{T_m^2}\right)$ versus $1/T_m$. Frame of the activation energy of the desorption step with high and low limits

The activation energy of hydrogen desorption calculated from Figure 10 is approximately 220 kJ mol⁻¹. However, the dispersion range is between 200 kJ mol⁻¹ and 370 kJ mol⁻¹. Figure 10 also shows that the dispersion between experiments conducted at the same heating rate increased when the heating rate decreased. Eq. 13. results from the assumption that diffusion is very fast. However, diffusion may not be negligible for every heating rate. The use of a numerical model thus appeared as necessary. The hydrogen desorption process was therefore solved by FE using the Cast3M code.

In the present case, both diffusion of hydrogen in the bulk (using Eq.1 for D_{Hi} and Eq.8) and surface recombination reaction of hydrogen atoms into diatomic molecules (using Eq.11) were taken into account in the calculations. They were made using a 24 wt. ppm hydrogen mean concentration in the alloy. The desorption rate constant k_{des} dependence on the temperature follows an Arrhenius law, with the activation energy of desorption Ea_{des} , and a pre-exponential factor k_{des}^0 (Eq. 14):

$$k_{des} = k_{des}^0 \cdot \text{Exp}\left(-\frac{Ea_{des}}{RT}\right) \quad (\text{Eq. 14})$$

At first approximation, the pre-exponential factor of the desorption rate constant was set equal to $7.28 \times 10^6 \text{ m s}^{-1}$. Figure 11 represents the influence of the activation energy on the hydrogen

desorption rate. The blue continuous curve corresponds to the TDS experiment, while others correspond to simulations with activation energies varying from 220 to 260 kJ mol^{-1} . The experimental temperature ramp was set to 10 K min^{-1} .

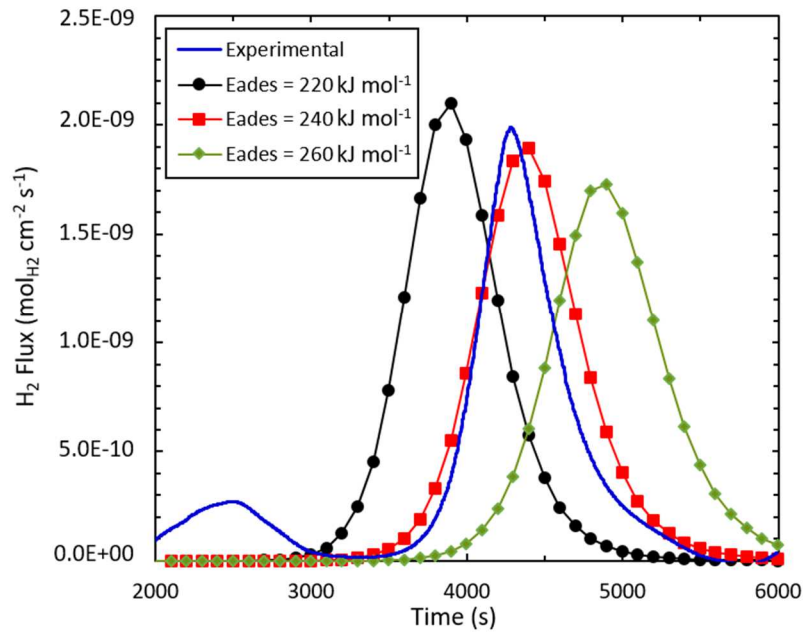


Figure 11. Comparison between simulated (dots) obtained by FE (Cast3M) and experimental (blue continuous line) H_2 desorption flux at 10 K min^{-1} with different $E_{a_{\text{des}}}$ values: 220 kJ mol^{-1} (black circles); 240 kJ mol^{-1} (red squares); 260 kJ mol^{-1} (green diamonds).

Figure 11 shows a strong influence of the activation energy on the hydrogen desorption kinetics. The red simulated curve with square markers well describes the experimental one in terms of maximum flux and peak position. For a pre-exponential factor, k_{des}° , equal to $7.28 \times 10^6 \text{ m s}^{-1}$, the best fit was obtained for an activation energy of about 240 kJ mol^{-1} . However, the Full Width at Half Maximum (FWHM) is too large compared with the experimental curve. Some adjustments are therefore needed, in order to refine the values of the couple $\{k_{\text{des}}^{\circ}, E_{a_{\text{des}}}\}$ and to optimize the fitting of experimental data.

In terms of peak maximum temperature and FWHM of the desorption peaks, the simulations carried out using the recombination rate constants assessed previously were not able to describe properly the TDS under a 10 K min^{-1} ramp, nor the other TDS performed at the two other different temperature ramps (not presented here). As a consequence, a numerical plan aiming at the

optimization of both coupled parameters of the recombination rate constant $\{k_{des}^{\circ}, E_{a_{des}}\}$ was undertaken: the URANIE software was used in this aim.

4.4.4 Seeking for the surface recombination kinetic constants

The "Uncertainty and Sensitivity" platform URANIE developed by the CEA aims to regroup methods and algorithms about Uncertainty and Sensitivity Analysis, Verification and Validation codes in the same framework [24]. URANIE is based on the data analysis framework ROOT, an object-oriented and petaflop computing system developed by CERN. URANIE was used to assess the activation energy ($E_{a_{des}}$) and the pre-exponential factor (k_{des}°) of the surface recombination rate constant.

Two URANIE tools were used in this study: the sampler and the optimizer libraries. The sampler library is developed to generate a design of experiment (deterministic/statistical) from $E_{a_{des}}$ and k_{des}° variables. In this study, the methodology LHS (Latin Hypercube Sampling) was employed. This tool generates a dot matrix with random paired values $\{\ln(k_{des}^{\circ}), E_{a_{des}}\}$ as illustrated in Figure 12.

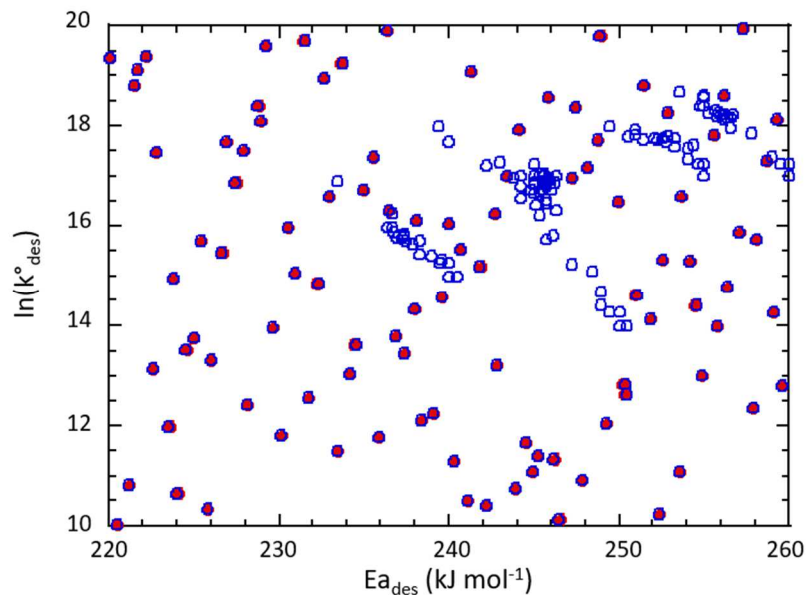


Figure 12. The initial dot matrix of random paired values of $E_{a_{des}}$ and k_{des}° (represented by $\ln(k_{des}^{\circ})$ here) obtained by the methodology LHS. The random paired values are the red circles surrounded by blue and the "local" optimization are represented by the blue empty circles.

For each pair of values and each temperature ramp (3 K min^{-1} , 7 K min^{-1} and 10 K min^{-1}), the FE code (Cast3M) simulates the associated hydrogen TDS thermogram. Then the normalized squared difference between the calculated data and experimental ones (indexed with the subscript "i") is calculated by Cast3M using the following formula (Eq. 15):

$$RR_i = \frac{\sum_j (F_{simu}(x_j) - F_{exp}(x_j))^2}{\max(\sum_k (F_{simu}(x_k))^2, \sum_l (F_{exp}(x_l))^2)} \quad (\text{Eq. 15})$$

Where RR_i is called a partial “error” criterion for experiment “i”, $F_{simu}(x_j)$ and $F_{exp}(x_l)$ are the simulated flux at the abscissa x_j and the experimental one at abscissa x_l , respectively. Subscripts “i” ($i \in \{1;2;3;4;5\}$) refer to following experiments: {1} for the 10 K min⁻¹ TDS, {2} for the first 7 K min⁻¹ TDS, {3} for the second 7 K min⁻¹ TDS, {4} for the first 3 K min⁻¹ TDS and {5} for the second 3 K min⁻¹ TDS. A global error criterion called RESULTAT was defined and corresponds to the RR_i sum (Eq. 16):

$$RESULTAT = \sum_{i=1}^{i=5} RR_i \quad (\text{Eq. 16})$$

The second tool, optimizer library, performs multi-criteria optimization with Genetic Algorithms allowing finding a local minimum of RESULTAT from a given initial value of the recombination rate constant pair (see the blue empty circles in Figure 12).

The first investigated domain of values ranged between 220 and 280 kJ mol⁻¹ for $E_{a_{des}}$ and between 10 and 22 for $\ln(k^{\circ}_{des})$. The initially investigated range does not allow to locate the global minimum at the first domain boundary. Therefore, the range for $E_{a_{des}}$ was extended up to 350 kJ mol⁻¹; the range for $\ln(k^{\circ}_{des})$ was extended to 32. Figure 13 represents the 3D map of RESULTAT function of $E_{a_{des}}$ and $\ln(k^{\circ}_{des})$. A valley of local minima is evidenced, and a linear regression between $E_{a_{des}}$ and $\ln(k^{\circ}_{des})$ in the minima valley is highlighted (see thick red dots in Figure 14, showing only those for which $RESULTAT < 0.5$). This suggests that a projection of the 3D map of RESULTAT on the $E_{a_{des}}$ axis should be equivalent in terms of minimization of the error to a projection on the $\ln(k^{\circ}_{des})$ axis.

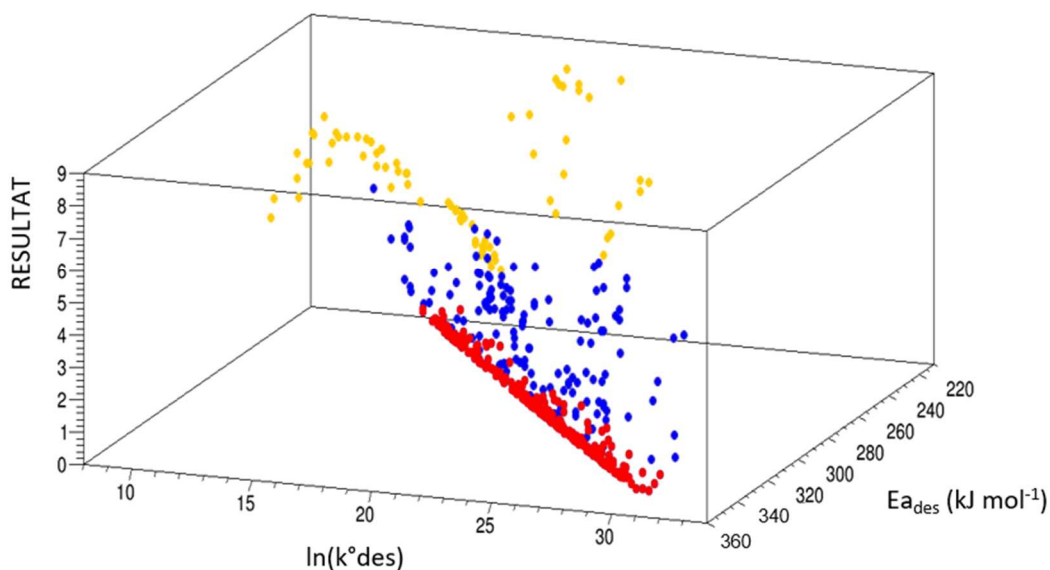


Figure 13. 3D map of RESULTAT versus $\ln(k^{\circ}_{des})$ and Ea_{des} in the range of [10, 32] and [220, 350], respectively : thick red dots for RESULTAT < 0.5, blue dots for 0.5 < RESULTAT < 5 and yellow dots for 5 < RESULTAT < 9.

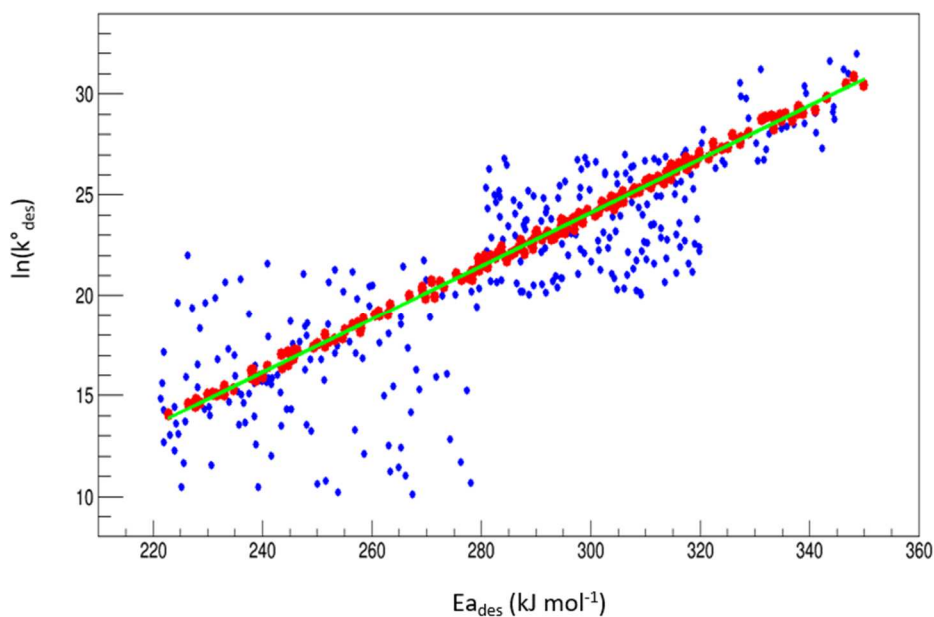


Figure 14. $\ln(k^{\circ}_{des})$ and Ea_{des} dependence for RESULTAT < 0.5 (thick red dots) and 0.5 < RESULTAT < 5 (bleu dots) with in continuous line the linear function between $\ln(k^{\circ}_{des})$ and Ea_{des} and in dashed lines the uncertainties of these paired values.

The resulting projection of RESULTAT 3D map on the Ea_{des} axis is presented in Figure 15. It shows unambiguously a global minimum for an activation energy around $290 \pm 10 \text{ kJ mol}^{-1}$, paired via the linear regression to a value for k°_{des} of $\exp(23 \pm 1) \text{ m s}^{-1}$ ($k^{\circ}_{des} = 9.7 \times 10^9 \text{ m s}^{-1}$).

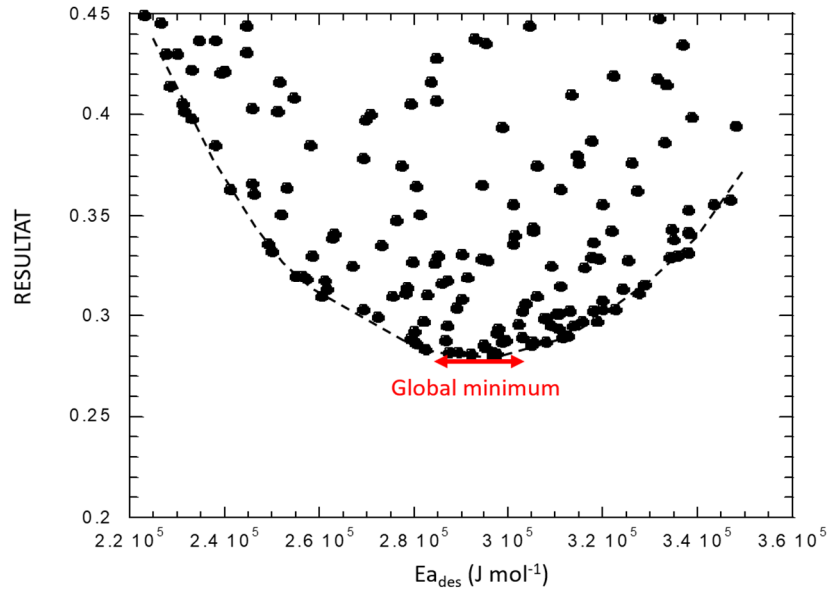


Figure 15. Projection of RESULTAT on Ea_{des} axis in the [220, 350] kJ mol^{-1} range.

It is also possible using the URANIE tools to determine the global minimum of the error criterion for each experiment. Table 3 presents the paired values of Ea_{des} and $\ln(k^{\circ}_{des})$ corresponding to the global minimum for each experiment.

Table 3. Paired values of Ea_{des} and $\ln(k^{\circ}_{des})$ corresponding to the global minimum for each experiment.

	Temperature ramp rate (K min^{-1})	Ea_{des} (kJ mol^{-1})	$\ln(k^{\circ}_{des})$	k°_{des} (m s^{-1})
Experiment 1 (RR1)	10	240 ± 10	16.5 ± 1.5	1.5×10^7
Experiment 2 (RR2)	7	320 ± 5	25 ± 1.5	7.2×10^{10}
Experiment 3 (RR3)	7	285 ± 5	22.2 ± 1	4.4×10^9
Experiment 4 (RR4)	3	330 ± 5	25.9 ± 1	1.8×10^{11}
Experiment 5 (RR5)	3	300 ± 5	23.8 ± 1.5	2.2×10^{10}

It appears that there is a large difference of optimized values for the 10 K min^{-1} ramp experiment and the first 3 K min^{-1} ramp one.

This final set of optimized values ($Ea_{des} = 290 \text{ kJ mol}^{-1}$ and $k^{\circ}_{des} = 9.7 \times 10^9 \text{ m s}^{-1}$) was then used to simulate the five TDS experiments and injected in the FE code. Figure 16 compares the TDS

desorption curves, simulated with these recombination kinetic constants (in red dot line) with experimental data (in blue continuous line), for all the investigated ramp rates.

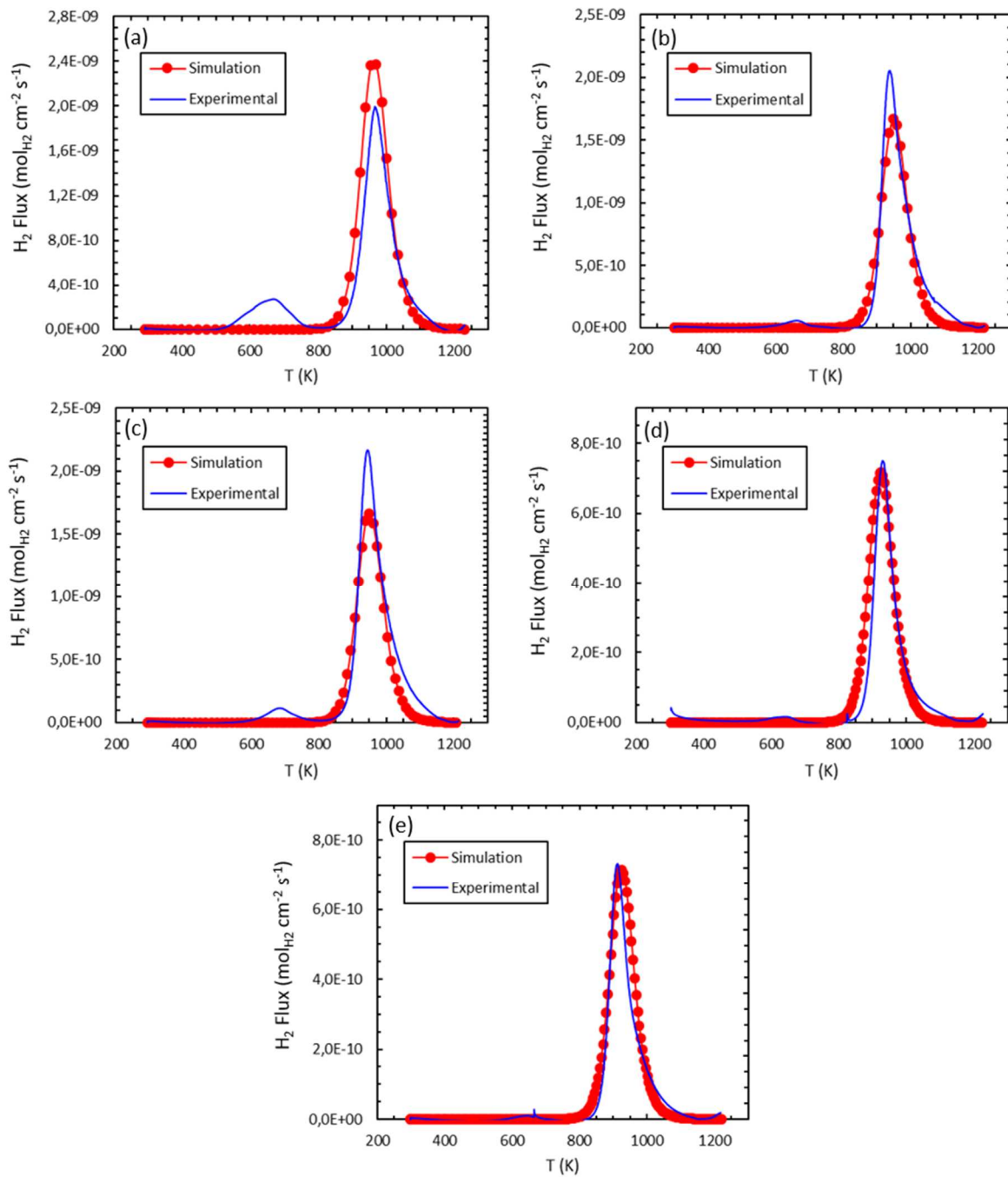


Figure 16. Comparison between simulated with the paired values $E_{a_{des}} = 290 \text{ kJ mol}^{-1}$ and $k^{\circ}_{des} = 9.7 \times 10^9 \text{ m s}^{-1}$ (red dots) and experimental (blue line) H_2 desorption flux obtained by FE calculations (Cast3M code) and TDS for different temperature ramps: (a) 10 K min^{-1} ; (b) 7 K min^{-1} - first experiment; (c) 7 K min^{-1} - second experiment; (d) 3 K min^{-1} - first experiment; (e) 3 K min^{-1} - second experiment.

The good agreement, in terms of shape, peak position and peak FWHM, between experimental data and simulation using this set of recombination kinetic constants, whatever the experiment or the temperature ramp chosen, shows the reliability of the determined $\{E_{a_{des}}; \ln(k^{\circ}_{des})\}$ pair values and the robustness of the method used.

In the literature, Baskes studied the hydrogen desorption kinetics from pure zirconium [18]. Table 4 compares the desorption flux φ_{H_2} calculated in the present study with those determined by Baskes [18]. The desorption fluxes in this study are calculated with Eq. 11. ($E_{a_{des}} = 290 \text{ kJ mol}^{-1}$, $k^{\circ}_{des} = 9.74 \times 10^9 \text{ m s}^{-1}$). Table 4 shows the desorption flux at 773 K, 873 K and 973 K for $C_H^{init} = 156 \text{ mol m}^{-3}$ and a Zy4 thickness equal to 180 μm .

Table 4. Comparison with the literature of the hydrogen desorption flux φ_{H_2} ($\text{mol m}^{-2} \text{ s}^{-1}$).

	Present study	Baskes [18]
773 K	5.5×10^{-9}	7.3×10^{-6}
873 K	1×10^{-6}	2×10^{-4}
973 K	1.1×10^{-4}	2×10^{-3}

Values presented in Table 4 show that the hydrogen desorption fluxes from Baskes' modelling are very different from those of our study (1 to 3 orders of magnitude). This difference is however lower at high temperature (i. e. 973 K). It is mainly due to the fact that our apparent activation energy of desorption process ($\sim 300 \text{ kJ mol}^{-1}$) is much higher than the one used in Baskes' modelling ($\sim 100 \text{ kJ mol}^{-1}$). In Baskes's approach, the energy paths of hydrogen to pass from the bulk metal to the desorbed state as a diatomic molecule are only based on thermodynamic considerations in terms of dissolution enthalpy in the metal (from free H_2 to solute H in the metal) and diffusion enthalpy in the metal lattice. Wilde's works [19], based on combined flash TDS and NRA measurements, show that desorption from the metal, e.g. Ti in [19], is by far more complex and includes additional energetically favored steps (leading the H atoms in metastable energy levels lower and lower from bulk to surface) for hydrogen to pass from the lattice to subsurface sites, then to surface sites. In such description proposed by Wilde et al., the energy barrier to overcome desorption (and surface molecular recombination) may be much higher than usually proposed based only on dissolution enthalpy considerations, modulated by diffusion enthalpy.

4.4.5 Challenging the model

In order to challenge our hydrogen desorption model, two additional TDS experiments were conducted following a more complex thermal history. A specific TDS procedure was adopted, including several isothermal plateaus. Between each isothermal plateau, a 10 K min^{-1} heating rate was applied. At the beginning of each experiment, an one-hour thermal treatment at 773 K was done in order to minimize the influence of the oxide scale formation due to the oxidation process involving chamber residual water described earlier in the paper; the specimen was then cooled down to room temperature in the vacuum chamber before pursuing the TDS experiment. The selected isothermal plateaus were: 773 K (15 min), 823 K (30 min), 853 K (1h) and 873 K (1h). The first quick step at 773 K enabled to check the cleanliness of the chamber and the occurrence of possible oxidation phenomena due to still-remaining water.

Figure 17 shows the experimental hydrogen desorption thermograms (black squares) obtained on an as-prepared not pre-oxidized Zy4 sheet (see section 2.1) following this dedicated TDS procedure. Results of FE simulations using a 24 wt. ppm hydrogen concentration and the paired values $E_{\text{des}} = 290 \text{ kJ mol}^{-1}$ and $k_{\text{des}}^{\circ} = 9.7 \times 10^9 \text{ m s}^{-1}$ and obtained by injecting directly in the code (Cast3M) the real temperature ramps applied to the specimen are shown in Figure 17 in red circles.

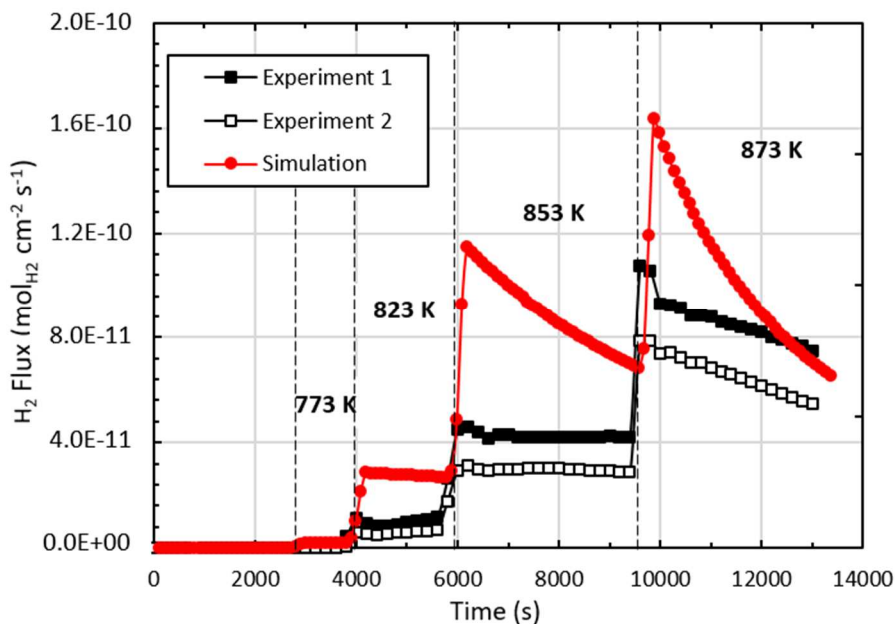


Figure 17. Comparison between simulated (red circles) and experimental (black squares) H_2 flux obtained by FE (Cast3M model) with the paired values $E_{\text{des}} = 290 \text{ kJ mol}^{-1}$ and $k_{\text{des}}^{\circ} = 9.7 \times 10^9 \text{ m s}^{-1}$ and TDS.

Simulation is very different from the experimental thermograms. This discrepancy can be due to either the uncertainties of the kinetic constant parameters ($E_{a_{des}}$, k°_{des}) or the initial hydrogen concentration within the material.

The initial hydrogen concentration was thus determined by the inert-gas melting extraction technique (using thermal conductivity in a Galileo G8 from Bruker) on a set of 10 specimens: the average concentration measured was 25 ± 5 wt.ppm (dispersion was attributed to sampling and not to error of the technique). The initial homogeneously distributed concentration of hydrogen in the Zy4 sheet was taken as an adjustment parameter (due to the potential variability of hydrogen distribution along the Zy4 sheet) and tested in the [20; 30] wt.ppm range. Since k'_{des} is independent of the initial hydrogen concentration unlike k_{des} , the concentration variation causes a modification of the pre-exponential factor k°_{des} (cf. Eq. 12). We also noticed that, except for the 10 K min^{-1} ramp rate, the average activation energy is closer to 300 kJ mol^{-1} . Simulations were carried out with this higher value than the previous solve (290 kJ mol^{-1}). As observed in Figure 18, better adjustments were obtained for 24 wt.ppm of hydrogen and $k^{\circ}_{des} = \exp(23) \text{ m s}^{-1}$ (empty green circles) and for 30 wt.ppm of hydrogen and $k^{\circ}_{des} = \exp(23.23) \text{ m s}^{-1}$ (full red circles).

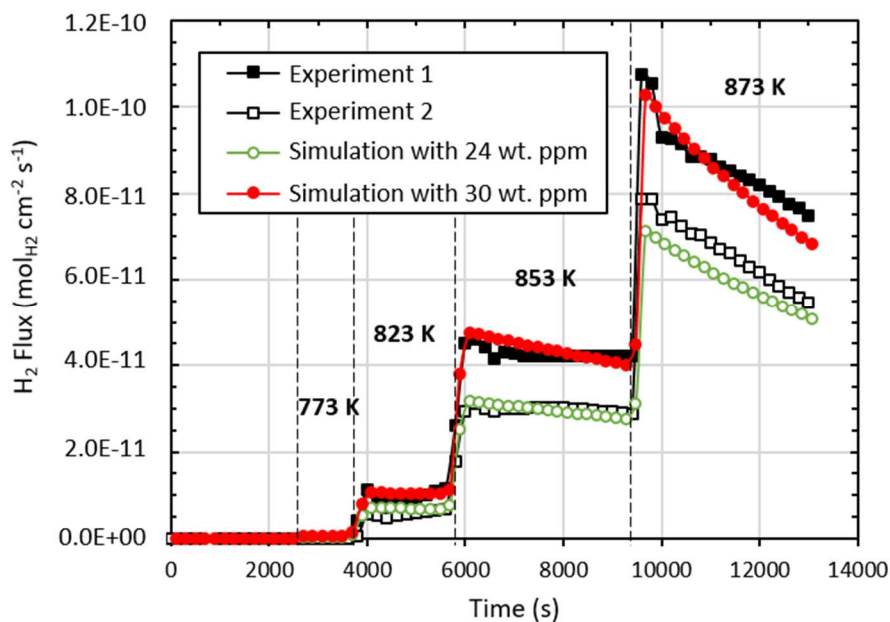


Figure 18. Comparison between simulated (red circles) and experimental (black squares) H_2 flux obtained by FE (Cast3M model) with the paired values $E_{a_{des}} = 300 \text{ kJ mol}^{-1}$ and $k^{\circ}_{des} = \exp(23) \text{ m s}^{-1}$ for 24 wt. ppm and $\exp(23.23) \text{ m s}^{-1}$ for 30 wt. ppm and TDS, respectively.

A global good agreement is found between simulation and experiments, giving more credit to the model proposed (bulk diffusion but surface recombination kinetically-controlled desorption rate), the

values obtained – and thus the methodology to assess them – as well as the way to solve it by finite elements.

5 Conclusion

The hydrogen desorption process from an unoxidized Zircaloy-4 specimen has been evaluated through thermal desorption spectrometry tests and by using modelling programmed with Cast3M code and URANIE optimization tool. The results of these investigations are consistent with the following conclusions:

1. The hydrogen desorption kinetics from the metal is limited by the surface recombination $2H_{ads} \rightarrow H_2$. The surface reaction is a second-order equation (Eq.10).
2. By coupling the Cast3M code with URANIE optimization platform, it is possible to optimize the error between the experimental spectra and the simulated ones and finally get the best-fitted setting of the kinetic constant k'_{des} , of the surface recombination step, which is expressed as follows (Eq. 17) :

$$k'_{des} = 3 \times 10^7 \cdot \exp\left(-\frac{2.90 \times 10^5}{RT}\right) \quad (\text{m}^4 \text{mol}^{-1} \text{s}^{-1}) \quad (\text{Eq. 17})$$

The impact of the presence of a significant oxide scale (pre-oxidized specimen) on desorption kinetics (barrier effect, recombination kinetics, rate-limiting step, etc.) will be studied later in future works. The integration of the oxide scale effect is also planned in our hydrogen desorption model (Cast3M) to determine the new rate limiting step for the complete system, more representative to “reality”.

This study illustrates the fact that interfacial reactions may be rate limiting even in the absence of oxide layer. This is a positive statement for safety considerations. Another important outcome of the present work is that researchers dealing with hydrogen permeation or desorption under the form of gas phase, who generally consider *a priori* the system in the frame of a diffusion rate limited problem, should be very careful and verify that such assumption remains valid and applicable to the studied system.

6 Acknowledgements

The authors want to thank CEA for funding this research and FRAMATOME for supplying the studied material.

7 References

- [1] IAEA, Waterside corrosion of zirconium alloys in nuclear power plants, Int. At. Energy Agency. TECDOC-996 (1998).
- [2] R.L. Tapping, X-ray photoelectron and ultraviolet photoelectron studies of the oxidation and hydriding of zirconium, *J. Nucl. Mater.* 107 (1982) 151–158.
- [3] G. Amsel, D. David, G. Beranger, P. Boisot, B. De Gelas, P. Lacombe, Analyse a l'aide d'une methode nucleaire des impuretes introduites dans les metaux par leurs preparations d'etat de surface: Application au zirconium, *J. Nucl. Mater.* 29 (1969) 144–153.
- [4] M. Tupin, F. Martin, C. Bisor, R. Verlet, P. Bossis, J. Chene, F. Jomard, P. Berger, S. Pascal, N. Nuns, Hydrogen diffusion process in the oxides formed on zirconium alloys during corrosion in pressurized water reactor conditions, *Corros. Sci.* 116 (2017) 1–13.
- [5] L. Afore, Etude du transport de l'hydrogene produit lors de la corrosion des gaines d'elements combustibles des reacteurs a eau sous pression dans la zircone et le zircaloy-4, Université de La Méditerranée Aix-Marseille II, 1997.
- [6] C. Bisor–Melloul, Compréhension des mécanismes de prise d'hydrogene des alliages de zirconium en situation de corrosion en conditions REP – Impact des hydrures sur la corrosion du Zircaloy-4, PhD Thesis, Université d'Evry, 2010.
- [7] E. Hillner, Hydrogen absorption in Zircaloy during aqueous corrosion, effect of environment, 1964.
- [8] M.W. Mallet, W.M. Albrecht, *J Electrochem Soc.* 104 (1957).
- [9] C.R. Cupp, P. Flubacher, An autoradiographic technique for the study of tritium in metals and its application to diffusion in zirconium at 149° to 240° C, *J. Nucl. Mater.* 6 (1962) 213–228.
- [10] G.U. Greger, H. Münzel, W. Kunz, A. Schwierczinski, Diffusion of tritium in zircaloy-2, *J. Nucl. Mater.* 88 (1980) 15–22.
- [11] A. Sawatzky, The diffusion and solubility of hydrogen in the alpha phase of Zircaloy-2, *J. Nucl. Mater.* 2 (1960) 62–68.
- [12] C. Schwartz, M. Mallet, Observation of the behavior of hydrogen in zirconium, *Trans. Am. Soc. Met.* 46 (1954) 641–654.
- [13] B.F. Kammenzind, D.G. Franklin, H.R. Peters, W.J. Duffin, Hydrogen Pickup and redistribution in alpha annealed Zircaloy-4, *Zircon. Nucl. Ind. 11th Int. Symp. ASTM STP 1295.* (1996) 338.
- [14] C.-S. Zhang, B. Li, P.R. Norton, The study of hydrogen segregation on Zr(0001) and Zr(1010) surfaces by static secondary ion mass spectroscopy, work function, Auger electron spectroscopy and nuclear reaction analysis, *J. Alloys Compd.* 231 (1995) 354–363.
- [15] J.H. Austin, T.S. Elleman, K. Verghese, Tritium diffusion in zircaloy-2 in the temperature range –78 to 204° C, *J. Nucl. Mater.* 51 (1974) 321–329.
- [16] I. Takagi, K. Une, S. Miyamura, T. Kobayashi, Deuterium diffusion in steam-corroded oxide layer of zirconium alloys, *J. Nucl. Mater.* 419 (2011) 339–346.
- [17] W. Kunz, H. Münzel, U. Kunz, Tritium release from Zircaloy-2: Dependence on temperature, surface conditions and composition of surrounding medium, *J. Nucl. Mater.* 136 (1985) 6–15.

- [18] M.I. Baskes, A calculation of the surface recombination rate constant for hydrogen isotopes on metals, *J. Nucl. Mater.* 92 (1980) 318–324.
- [19] M. Wilde, K. Fukutani, Penetration mechanisms of surface-adsorbed hydrogen atoms into bulk metals: Experiment and model, *Phys. Rev. B.* 78 (2008). doi:10.1103/PhysRevB.78.115411.
- [20] I.S. Dupim, J.M.L. Moreira, J. Huot, S.F. Santos, Effect of cold rolling on the hydrogen absorption and desorption kinetics of Zircaloy-4, *Mater. Chem. Phys.* 155 (2015) 241–245. doi:10.1016/j.matchemphys.2015.02.036.
- [21] J. Sayers, S. Ortner, S. Lozano-Perez, Effect of pH on hydrogen pick-up and corrosion in zircaloy-4, *Miner. Met. Mater. Ser. Part F9* (2018) 1169–1180.
- [22] www-cast3m.cea.fr/, (n.d.).
- [23] G. Zumpicchiati, S. Pascal, M. Tupin, C. Berdin-Méric, Finite element modelling of the oxidation kinetics of Zircaloy-4 with a controlled metal-oxide interface and the influence of growth stress, *Corros. Sci.* 100 (2015) 209–221.
- [24] F. Gaudier, URANIE: The CEA/DEN Uncertainty and Sensitivity platform, *Procedia - Soc. Behav. Sci.* 2 (2010) 7660–7661.
- [25] W.Y. Choo, J.Y. Lee, Thermal analysis of trapped hydrogen in pure iron, *Metall. Trans. A.* 13 (1982) 135–140.
- [26] W.Y. Choo, J.Y. Lee, Hydrogen trapping phenomena in carbon steel, *J. Mater. Sci.* 17 (1982) 1930–1938.
- [27] T. Kasuya, M. Fuji, Diffusion with multiple kinds of trapping sites, *J. Appl. Phys.* 83 (1998) 3039–3048.
- [28] C. Hurley, F. Martin, L. Marchetti, J. Chêne, C. Blanc, E. Andrieu, Numerical modeling of thermal desorption mass spectroscopy (TDS) for the study of hydrogen diffusion and trapping interactions in metals, *Int. J. Hydrog. Energy.* 40 (2015) 3402–3414.
- [29] C. Morant, J.M. Sanz, L. Galán, L. Soriano, F. Rueda, An XPS study of the interaction of oxygen with zirconium, *Surf. Sci.* 218 (1989) 331–345.
- [30] I. Bepalov, M. Datler, S. Buhr, W. Drachsel, G. Rupprechter, Y. Suchorski, Initial stages of oxide formation on the Zr surface at low oxygen pressure: An in situ FIM and XPS study, *Ultramicroscopy.* 159 (2015) 147–151.
- [31] A.J. Machiels, Corrosion of Zircaloy-clad LWR fuel rods, 1987.
- [32] M. Benoit, C. Bataillon, B. Gwinner, F. Miserque, M.E. Orazem, C.M. Sánchez-Sánchez, B. Tribollet, V. Vivier, Comparison of different methods for measuring the passive film thickness on metals, *Electrochimica Acta.* 201 (2016) 340–347.
- [33] W.H. Gries, A Universal Predictive Equation for the Inelastic Mean Free Pathlengths of X-ray Photoelectrons and Auger Electrons, *Surf. Interface Anal.* 24 (1996) 38–50.
- [34] Z. Song, X. Bao, U. Wild, M. Muhler, G. Ertl, Oxidation of amorphous Ni–Zr alloys studied by XPS, UPS, ISS and XRD, *Appl. Surf. Sci.* 134 (1998) 31–38.
- [35] M. Andersson, S. Urbonaitė, E. Lewin, U. Jansson, Magnetron sputtering of Zr–Si–C thin films, *Thin Solid Films.* 520 (2012) 6375–6381.
- [36] P.E. West, P.M. George, An x-ray photoelectron spectroscopy investigation of the incorporation of surface oxides into bulk zirconium, *J. Vac. Sci. Technol. Vac. Surf. Films.* 5 (1987) 1124–1127.
- [37] I.G. Ritchie, A. Atrens, The diffusion of oxygen in alpha-zirconium, *J. Nucl. Mater.* 67 (1977) 254–264.
- [38] D. Quataert, F. Coen-Porisini, Utilization of the ion analyser for the study of oxygen diffusion in solids and its application to zirconium, *J. Nucl. Mater.* 36 (1970) 20–28.
- [39] B. Li, A.R. Allnatt, C.-S. Zhang, P.R. Norton, Model and theory for the determination of diffusion coefficients by Auger electron spectroscopy measurements and an application to oxygen diffusion along the [0001] and [101̄0] axes in single crystal zirconium, *Surf. Sci.* 330 (1995) 276–288.
- [40] M. Parise, Mécanismes de corrosion des alliages de zirconium : étude des cinétiques initiales d'oxydation et du comportement mécanique du système métal – oxyde, Ecole Nationale Supérieure des Mines de Paris, 1996.

- [41] K. Une, S. Ishimoto, Terminal Solid Solubility of Hydrogen in Unalloyed Zirconium by Differential Scanning Calorimetry, *J. Nucl. Sci. Technol.* 41 (2004) 949–952.
doi:10.1080/18811248.2004.9715569.
- [42] H.E. Kissinger, Reaction kinetics in differential thermal analysis, *Anal. Chem.* 29 (1957) 1702–1706.